ADVANCED OPTICAL MATERIALS
www.advopticalmat.de

Modeling and Improving Geometric Accuracy in Projection Multiphoton Lithography

*Anwarul Islam Akash, Jason E. Johnson, and Xianfan Xu**

Projection multiphoton lithography (PMPL) is a promising alternative to conventional voxel-by-voxel serial writing lithography, offering significant gain in fabrication speed. However, this high throughput can come at the expense of geometric accuracy, as printed structures can deviate from the intended patterns displayed on the digital micromirror device (DMD). To uncover the origins of these deviations, a numerical framework is developed that solves coupled 3D reaction-diffusion equations and captures the underlying photochemical processes of projection-based printing. Simulations of elementary geometries such as circles and rectangles, which serve as building blocks of complex architectures, reveal that oxygen inhibition, oxygen diffusion from surrounding regions, and intensity variations due to DMD diffraction are the dominant sources of geometric distortion. Guided by these insights, pre-exposure and asymmetric compensation strategies are proposed that modify the projected patterns to counteract these effects. Simulations and experiments indicate that these approaches hold promise for mitigating distortions and improving the fidelity of printed structures, offering a pathway toward more accurate, high-throughput 3D microfabrication.

1. Introduction

Two-photon polymerization (TPP) using a femtosecond laser, also referred to as multiphoton polymerization (MPP), is a light-based additive manufacturing (AM) technique capable of fabricating complex 3D structures with sub-micron features by leveraging the nonlinear nature of multiphoton absorption.[1–4] Offering exceptional design freedom and nanoscale prototyping capabilities, MPP has been applied across diverse fields, including optics and photonics,[5–7] microrobotics,[8,9] bioengineering,[10,11] and metamaterials.[12,13] Despite its superior resolution and geometric accuracy, the widescale adoption of MPP in industrial applications remains limited due to the inherently slow throughput of conventional voxel-by-voxel serial writing. To overcome this limitation, strategies have been developed that can boost fabrication speed by several orders of magnitude, like multi-foci scanning enabled by a diffractive optical element[14] or holography[15,16] and projection multiphoton lithography (PMPL).[17,18]

The strategy of projecting an entire layer at once to increase throughput has been successfully demonstrated with single-photon polymerization, achieving resolutions ranging from ≈0.6 to 100 µm depending on the printed structure.[19–21] Efforts to realize projection-based MPP while preserving consistent sub-micrometer resolution have prompted the development of several approaches, primarily involving the use of gratings to induce dispersion and subsequent spatiotemporal focusing of the laser pulse for improved axial confinement of intensity.[22,23] More recently, the implementation of DMDs has simplified the optical setup by combining the dispersive component and spatial amplitude modulation into one device, allowing for highly confined patterned polymerization within a very thin layer.[17,18] In PMPL, a high-intensity femtosecond laser beam is projected onto a DMD that patterns the beam according to the displayed 2D pattern, enabling the fabrication of an entire slice in a single exposure. The angular dispersion inherently introduced by the DMD stretches the pulse duration, resulting in insufficient intensity for MPP. However, at the print plane, the optical system recombines the dispersed spectral components and therefore compresses the pulse at the image plane, hence termed spatiotemporal focusing, achieving sufficient pulse intensity for printing only within a sub-micrometer region along the optical axis. While PMPL provides high throughput, geometric inaccuracies such as edge and corner feature loss[24–26] and structural asymmetry can be significant at the submicrometer level. Although these deviations are often attributed primarily to oxygen inhibition in serial writing,[27–29] additional contributing factors can be present in PMPL.

Addressing geometric inaccuracies requires a rigorous understanding of the fundamental sources of geometric deviations in PMPL and the development of systematic compensation strategies. A physics-based model that captures the underlying photopolymerization dynamics is therefore essential. Both empirical and physics-based models have been employed to describe various phenomena in serial writing,[27,30–33] and

A. I. Akash, J. E. Johnson, X. Xu
School of Mechanical Engineering and Birck Nanotechnology Center
Purdue University
1205 Mitch Daniels Blvd., West Lafayette, IN 47907, USA
E-mail: xxu@ecn.purdue.edu

The ORCID identification number(s) for the author(s) of this article can be found under https://doi.org/10.1002/adom.202503185

DOI: 10.1002/adom.202503185

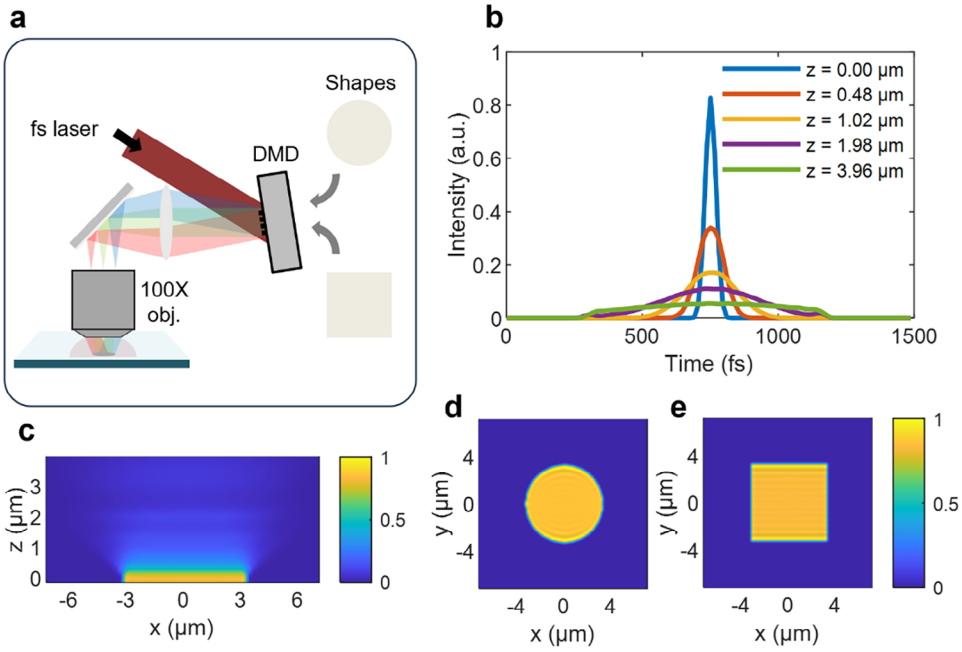

Figure 1. a) Simplified schematic of the projection printing experimental setup. b) Normalized temporal intensity distribution for selected axial *z*-positions at the optical axis center location ($x = 0$, $y = 0$). c) Spatiotemporal focusing of the normalized intensity distribution in the *x*-*z* plane ($y = 0$) for a 6.75 × 6.75 μm rectangular pattern, showing recombination of dispersed components at the print plane. d) Intensity distribution of a 6.75 μm diameter circle at the print plane ($z = 0$). e) Intensity distribution of a 6.75 × 6.75 μm rectangle at the print plane ($z = 0$). Subfigures (d) and (e) share a common colorbar.

micro-stereolithography,[25] while lumped parametric models combined with predictive algorithms and precompensation strategies have been used to improve geometric fidelity.[34,35] Although existing modeling efforts in PMPL provide valuable foundations, they do not adequately capture the influence of oxygen inhibition and other process parameters on geometric deviations, nor do they explore potential strategies for systematic mitigation.[36,37]

In PMPL, sequentially projected 2D patterns are stacked to form the final 3D structure. Ideally, each layer should exhibit a flat, uniform profile. However, in practice, edges tend to under-polymerize, resulting in a dome-like layer with rounded corners, asymmetric shrinkage, and other distortions. Consequently, achieving high-fidelity 3D structures requires improving the accuracy of the microstructures generated from each 2D layer. Data-driven approaches have recently demonstrated effectiveness in this regard. Bayesian optimization with Gaussian-process-based active machine learning,[26] and convolutional autoencoder frameworks,[38] have successfully compensated for corner rounding and dimensional inaccuracies in 2D layers, occurring primarily due to oxygen inhibition, yielding substantial improvements in 2D accuracy. Despite these advances, at present, machine learning based approaches remain limited in their ability to capture the underlying physics responsible for geometric inaccuracies in PMPL. To address this gap, in this work, we present a numerical framework that incorporates the optical and photochemical processes involved in the spatiotemporally focused projection-based 3D printing. The optical model accounts for the angular dispersion introduced by the DMD, leading to temporal focusing at the print plane and the diffraction effect that induces intensity variations across the projected pattern.[18] The photochemical model numerically solves the coupled reaction-diffusion equations describing photopolymerization kinetics, allowing us to track the time-dependent concentrations of reaction species during the fabrication of circles and rectangles under varying intensity and exposure conditions. We demonstrate that this model is capable of capturing the size dependence of the threshold dose and of accurately simulating the printed 3D profiles of various 2D patterns. Moreover, this model allows us to further investigate the role of oxygen diffusion, demonstrating that local oxygen inhibition and diffusion from the surrounding regions lead to corner rounding and feature under-polymerization, while the interaction between DMD diffraction and oxygen inhibition produces asymmetric distortions. Building on these insights, we propose general compensation strategies, including pre-exposure and asymmetric pattern modifications, that adjust the projected DMD patterns to improve the geometric accuracy of printed structures.

2. Modeling Framework

2.1. Optical Field Propagation

A simplified schematic of the experimental setup is presented in **Figure 1a**, following the configuration reported previously.[26] A 12 mm diameter beam from a Ti-sapphire regenerative amplifier operating at 5 kHz repetition rate, 800 nm center wavelength, and 30 nm bandwidth is incident on a DMD, which operates as both a pattern generator and a diffraction grating. The dispersed beam from the DMD is then collected by a lens and

relayed to the back focal plane of a 100× oil immersion objective (see the Experimental Section). Spatiotemporal focusing is achieved because both the pattern and dispersion originate from the same conjugate plane at the DMD. With the collector lens and the objective lens in a 4f configuration, this arrangement recombines the dispersed spectral components of the laser pulse at the print plane, submerged in a liquid photoresist. The photoresist mixture consists of monomer pentaerythritol triacrylate (PETA) with 0.38 mol% (2E,6E)-2,6-Bis (4-(dibutylamino) benzylidene)-4-methylcyclohexanone (BBK) as photoinitiator.

A Fourier optics model can be employed to simulate the spatiotemporal propagation of a pulse through this system.[18] A scalar plane wave light field comprising frequencies ω with a Gaussian distribution is incident on the DMD as,

$$U_i\ (x, y, \omega) = Ae^{\frac{(\omega-\omega_0)^2}{\Omega^2}} \tag{1}$$

where A is the amplitude, (x,y) are the DMD spatial coordinates, ω_0 is the central frequency, and Ω denotes the spectral full width at half maximum (FWHM). Treating the DMD as a 2D diffraction grating, the wavelength-dependent diffraction introduced by the DMD is applied to the light field as a phase term:[39]

$$\phi_{DMD} = e^{2\pi j x \frac{\sqrt{2}m}{d}\frac{(\lambda-\lambda_0)}{\lambda}} \tag{2}$$

where $m = 3$ is the diffraction order that satisfies both the grating equation and the specular reflection condition of the blazed grating, $d = 7.637$ µm is the DMD mirror pitch, and λ is the wavelength component of the light field centered at λ_0. The light field leaving the DMD is then given by,

$$U_d\ \left(x_d, y_d, \omega\right) = U_i\ (x, y, \omega)\, H\,(x, y)\, \phi_{DMD} \tag{3}$$

where $H(x,y)$ is the binary mask representing the projected DMD pattern. The subsequent propagation through the collecting lens, U_A, and an objective lens, U_f, is obtained using the Fourier transforming properties of lenses and the angular spectrum method.[40]

$$U_A\ \left(x_A, y_A, \omega\right) = -\frac{j}{\lambda f_1}\mathcal{F}\left\{U_d\left(x_d, y_d, \omega\right)\right\} \tag{4}$$

$$U_f\ \left(x_f, y_f, z, \omega\right) = \frac{-jn}{\lambda f_2}\, e^{j\frac{2\pi n}{\lambda}(2f_2+z)}\mathcal{F}\left\{U_A\left(x_A, y_A, \omega\right) P e^{-j\frac{\pi z n}{\lambda f_2^2}\left({x_A}^2+{y_A}^2\right)}\right\} \tag{5}$$

where $\mathcal{F}\{\cdot\}$ denotes the Fourier transformation, f_1 and f_2 are the focal lengths of the collecting and objective lenses, respectively, P is the pupil function describing the back aperture of the objective lens, n is the refractive index of the photoresist, and z is the distance from the print plane.

Using this system of equations, the spectral and temporal intensity profiles corresponding to any DMD pattern can be simulated. Since temporal focusing and pulse front tilt from the DMD cause both the pulse duration and the pulse arrival time to vary across the 4D domain (x, y, z, t), the optical model extracts the time-resolved intensity profile at each spatial location. To efficiently represent this information, the effective pulse arrival time is tracked using the temporal center of mass of the local intensity profile. A 1500 fs time window centered on this point is then recorded, which ensures that the entire spatiotemporal pulse structure is captured consistently at each pixel while avoiding unnecessary data inflation. Since the timescale of the pulse front tilt is small relative to the timescale of the polymerization reaction, we assume it has minimal effect and center all the temporal pulse profiles within a 1500 fs window to allow for significant compression of the time dimension of the 4D intensity array. The resulting profile is then used in the photopolymerization model described in the next section.

Figure 1b shows the calculated normalized temporal intensity profiles at the optical axis center ($x = 0$, $y = 0$) for selected axial z-positions. Away from the print plane ($z = 0$), the pulse undergoes temporal stretching, resulting in a reduced peak intensity. This behavior highlights how spatiotemporal focusing confines the pulse energy at the focal plane, while the chosen 1500 fs time window fully encompasses the pulse profile even at the most stretched spatial locations. Figure 1c demonstrates this effect by showing the calculated x-z spatiotemporal intensity distribution at $y = 0$ for a 6.75 × 6.75 µm rectangular pattern. The dispersed spectral components recombine at the print plane to achieve maximum intensity. The z-axial confinement of this distribution largely determines the thickness of each printed layer. Figure 1d,e shows the calculated intensity distributions at the print plane for two projected patterns: a 6.75 µm diameter circle and a 6.75 × 6.75 µm rectangle, respectively. In both cases, the distributions are evaluated at the midpoint of the time window, when each spatial location reaches its peak intensity, thereby confirming the temporal confinement of the pulse. However, the intensity distribution is not uniform across the entire pattern. Intensity variations along the y-direction arise from DMD diffraction, with the maximum intensity occurring at the top and bottom horizontal edges of the projected pattern.

2.2. Photochemical Kinetics

A numerical model was developed to describe the photochemical processes involved in PMPL. This model takes the patterned light intensity distribution from the optical model as an input and builds upon prior modeling work on serial writing,[30,31] extending it to projection-based systems. **Figure 2a** illustrates the modified Jablonski diagram, which incorporates the triplet absorption (TA) pathway recently proposed for the BBK photoinitiator.[41] The 800 nm fs laser induces simultaneous absorption of two photons from the ground state (S_0) to the excited singlet state (S_1). From S_1, molecules can either return to S_0 via fluorescence (Fl) or undergo intersystem crossing (ISC) to the lowest energy triplet state (T_1), depending on the triplet quantum efficiency of the photoinitiator. Molecules in the T_1 state can relax back to S_0 via phosphorescence (Ph) or nonradiative internal conversion, or they may participate in radical generation pathways depending on the photoinitiator type (Norrish type I or II). For the BBK photoinitiator in the absence of a co-initiator, it is proposed that the dominant process involves absorption of a third photon via TA to reach a higher energy triplet state (T_n). From T_n, BBK can generate radicals either through intermolecular hydrogen atom transfer (HAT) with the monomer PETA or via photolysis of carbon-carbon and carbon-nitrogen bonds.[41] Since BBK exhibits very weak self-deactivation,[42] the reverse intersystem

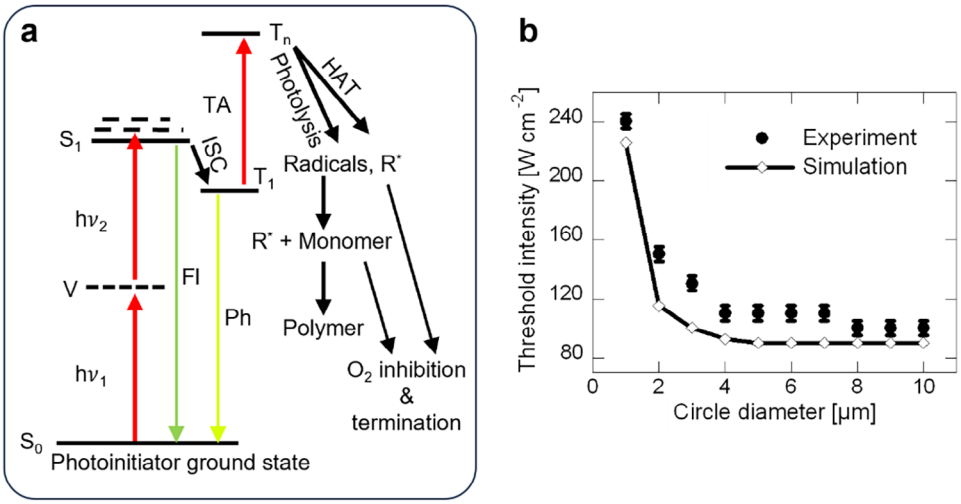

Figure 2. a) Modified Jablonski diagram considered for the model. From the ground state (S_0), photoinitiator molecules are excited to the singlet state (S_1) through two-photon absorption (TPA). From S_1, they can either relax back to S_0 via fluorescence (*Fl*) or undergo intersystem crossing (ISC) to reach the lowest energy triplet state (T_1). From T_1, the molecules can either return to the ground state through phosphorescence (*Ph*) or absorb another photon via triplet absorption (TA) to reach a higher-energy triplet state (T_n). From the T_n state, radicals are generated through both photolysis and intermolecular hydrogen atom transfer (HAT). These radicals then react with free monomers to initiate polymer chain formation or are terminated by oxygen. b) Threshold intensity measurements for circle diameters ranging from 1 to 10 μm, comparing simulated and experimental results. The threshold intensity is defined as the minimum average intensity below which no polymerized material is observed. Error bars on the experimental data represent the uncertainty associated with the discrete step size in intensity measurements (± step size/2).

crossing (RISC) pathway is not considered in the model. The generated radicals then react with free monomers to form macroradicals, initiating polymer chain growth, or are quenched through reactions with oxygen. Although radical generation directly from the T_1 state, as reported in earlier models,[30,31] can be incorporated in this framework, recent work suggests radical generation from the T_n state is the primary pathway for polymerization.[41] Therefore, we present this model with radical generation from the T_n state.

The chemical processes underlying photopolymerization can be described by a set of spatiotemporal concentration rate equations.[30,31,43] The equations are divided into two sections: (i) excitation kinetics of the photoinitiator through multiphoton and triplet absorption pathways, and (ii) subsequent radical-mediated polymerization reactions. The dynamics of the ground-state photoinitiator $[PI]$, the lowest triplet state $[T_1]$, and the higher triplet state $[T_n]$ are given by:[30,31]

$$\frac{\partial [PI]}{\partial t} = d_{PI}\nabla^2 [PI] - \phi_T \sigma_2 \Phi^2 [PI] + k_{ph} [T_1] \quad (6)$$

$$\frac{\partial [T_1]}{\partial t} = \phi_T \sigma_2 \Phi^2 [PI] - k_{ph} [T_1] - \frac{\varepsilon}{N_A} \Phi [T_1] \quad (7)$$

$$\frac{\partial [T_n]}{\partial t} = \frac{\varepsilon}{N_A} \Phi [T_1] - k_r [T_n] - k_{rpi} [T_n] \quad (8)$$

In Equation (6), the terms on the right-hand side represent photoinitiator diffusion, change of the ground state photoinitiator due to two-photon absorption (TPA) and fluorescence, and recovery due to phosphorescence, respectively. Here, d_{PI} is the photoinitiator diffusivity, ϕ_T the triplet quantum yield, σ_2 the TPA cross-section, $\Phi = I(x, y, z, t)/h\nu$ the photon flux, and k_{ph} the kinetic rate coefficient for phosphorescence. The S_1 state is not explicitly considered in the model since ISC is assumed to be instantaneous.[44] Thus, ϕ_T accounts for all the losses from the S_1 state through fluorescence and other nontriplet pathways.[45,46] The last term in Equation (7) describes the transition from T_1 to T_n via TA, where ε is the molar extinction coefficient and N_A Avogadro's number. Equation (8) includes radical generation pathways from the T_n state, where k_r and k_{rpi} are the kinetic rate coefficients for HAT and photolysis, respectively. The subsequent radical-mediated polymerization steps are captured by the following equations:[30,31,43]

$$\frac{\partial [R]}{\partial t} = k_r [T_n] + 4k_{rpi} [T_n] - k_i [R][M] - k_t [R][MR] - 2k_t [R]^2 - k_z [R][Z] \quad (9)$$

$$\frac{\partial [MR]}{\partial t} = k_r [T_n] + k_i [R][M] - k_t [R][MR] - 2k_t [MR]^2 - k_z [MR][Z] \quad (10)$$

$$\frac{\partial [Z]}{\partial t} = d_z \nabla^2 [Z] - k_z [R][Z] - k_z [MR][Z] \quad (11)$$

$$\frac{\partial [M]}{\partial t} = -k_i [R][M] - k_p [M][MR] - k_r [T_n] \quad (12)$$

$$\frac{\partial C}{\partial t} = k_i [R][M] + k_p [M][MR] + k_r [T_n] \quad (13)$$

Equations (9)–(12) describe the kinetics of radicals $[R]$, macroradicals $[MR]$, inhibitors (oxygen) $[Z]$, and free monomers $[M]$, respectively. BBK generates two radicals through HAT with the PETA monomer, yielding one ketyl radical on BBK and one alkyl radical on PETA. Furthermore, due to the two tertiary amine groups present in BBK, it is proposed that up to four radicals can be generated through photolysis.[41] Here, k_i, k_t, k_z, and k_p denote the kinetic rate coefficients for initiation, termination,

Table 1. Model Parameters.

Parameter	Symbol	Value	Source
Laser center wavelength		800 nm	Measured
Bandwidth		30 nm	Measured
Repetition rate		5 kHz	Measured
Pulse duration		40 fs	Measured
Beam diameter		12 mm	Measured
System (de)magnification		90	Measured
Average intensity		90.3–240.7 [W cm^{-2}]	Measured
Peak intensity		4.24×10^{11}–1.13×10^{12} [W cm^{-2}]	Measured
Free monomer initial concentration	$[M]_i$	3900 [mol m^{-3}]	Measured
Photoinitiator initial concentration	$[PI]_i$	15 [mol m^{-3}]	Measured
Inhibitor initial concentration	$[Z]_i$	6 [mol m^{-3}]	[27]
Triplet quantum yield	ϕ_T	0.90	[31,41]
Kinetic rate coefficient for initiation	k_i	50 [m^3 mol^{-1} s^{-1}]	[49]
Kinetic rate coefficient for termination	k_t	1 [m^3 mol^{-1} s^{-1}]	[50]
Kinetic rate coefficient for inhibition	k_z	3.82×10^4 [m^3 mol^{-1} s^{-1}]	[30,31,43]
Kinetic rate coefficient for phosphorescence	k_{ph}	8.94×10^4 [s^{-1}]	[41]
Kinetic rate coefficient for radical generation (HAT)	k_r	1.06×10^5 [s^{-1}]	[30,51]
Kinetic rate coefficient for radical generation (Photolysis)	k_{rpi}	1.06×10^4 [s^{-1}]	$\approx$ 0.1 k_r[41]
Photoinitiator diffusivity	d_{PI}	2.22×10^{-11} [m^2 s^{-1}]	[30]
Kinetic rate coefficient for propagation	k_p	100 [m^3 mol^{-1} s^{-1}]	114.5 [m^3 mol^{-1} s^{-1}][52]
Two-photon cross section	σ_2	200 [GM]	191 [GM][53]
Excited state molar extinction coefficient	ε	13 000 [$M^{-1}cm^{-1}$]	10 000 [$M^{-1}cm^{-1}$][54]
Oxygen diffusivity	d_z	7.48×10^{-10} [m^2 s^{-1}]	2.27×10^{-10} [m^2 s^{-1}][43]

inhibition, and propagation, respectively. The diffusivity of oxygen is represented by d_z in Equation (11), while the concentration of converted monomers is denoted by C in Equation (13). Recent work shows the possibility of nonlinear absorption by the monomer itself.[47] PETA monomer has been shown to induce polymerization via a highly nonlinear 7-photon photoionization process, using ≈25x higher fluence or ≈5x higher peak intensity compared to the present work (the absorption cross-section is unknown).[48] On the other hand, the two-photon cross-section of the BBK photoinitiator parent molecule is very large, as listed in **Table 1**. Therefore, the contribution of nonlinear absorption by PETA is expected to be negligible and is not considered in the present model.

All governing equations were solved numerically using the forward time centered space (FTCS) method implemented in MATLAB. The spatiotemporal concentration fields were discretized on a uniform grid with 0.06 μm spatial step size, determined by the DMD pixel spacing and system magnification. Time stepping was performed explicitly with a stability-limited step size of 0.1 μs, which is well within the Neumann stability criteria for explicit diffusion of both oxygen and photoinitiator, and sufficiently small to capture the temporal evolution of reaction species. A shorter time step of 15 fs was used during pulsed laser illumination. The PMPL process was simulated with a time-resolved intensity distribution over a 14.4 μm × 14.4 μm × 4.0 μm computational domain, which was sufficiently large to avoid boundary artifacts for the projected patterns. To simulate the presence of the substrate surface, no-flux Neumann boundary conditions were applied at $z = 0$, while fixed concentration Dirichlet boundary conditions were applied at all other boundaries for oxygen and photoinitiator diffusion. Table 1 summarizes the parameters used in the model along with their respective sources. Most parameters were either measured or taken from literature, while the last four parameters, kinetic rate coefficient for propagation, two-photon cross-section, excited state molar extinction coefficient, and oxygen diffusivity, were adjusted around reference values to reproduce both the intensity vs threshold relationship in Figure 2b and the height map profiles in **Figure 3**.

3. Results and Discussion

3.1. Experimental Characterization and Model Validation

In PMPL, patterned laser light from the DMD polymerizes the desired layer inside a liquid photosensitive resin, and 3D objects are fabricated by sequentially stacking these layers. To evaluate the model's ability to predict printability under varying intensity and exposure conditions, we conducted an experiment analogous to the threshold power vs exposure tests commonly reported in MPP literature.[27,43] Since PMPL uniquely enables printing of an entire layer in a single exposure, threshold intensity tests were performed on circles with diameters ranging from 1 to 10 μm. Immediately after printing, printability was assessed using the in-situ quantitative phase imaging (QPI) method.[55] For each diameter, with exposure fixed at 1100 μs, the average laser intensity was varied until no printed material was detected in the

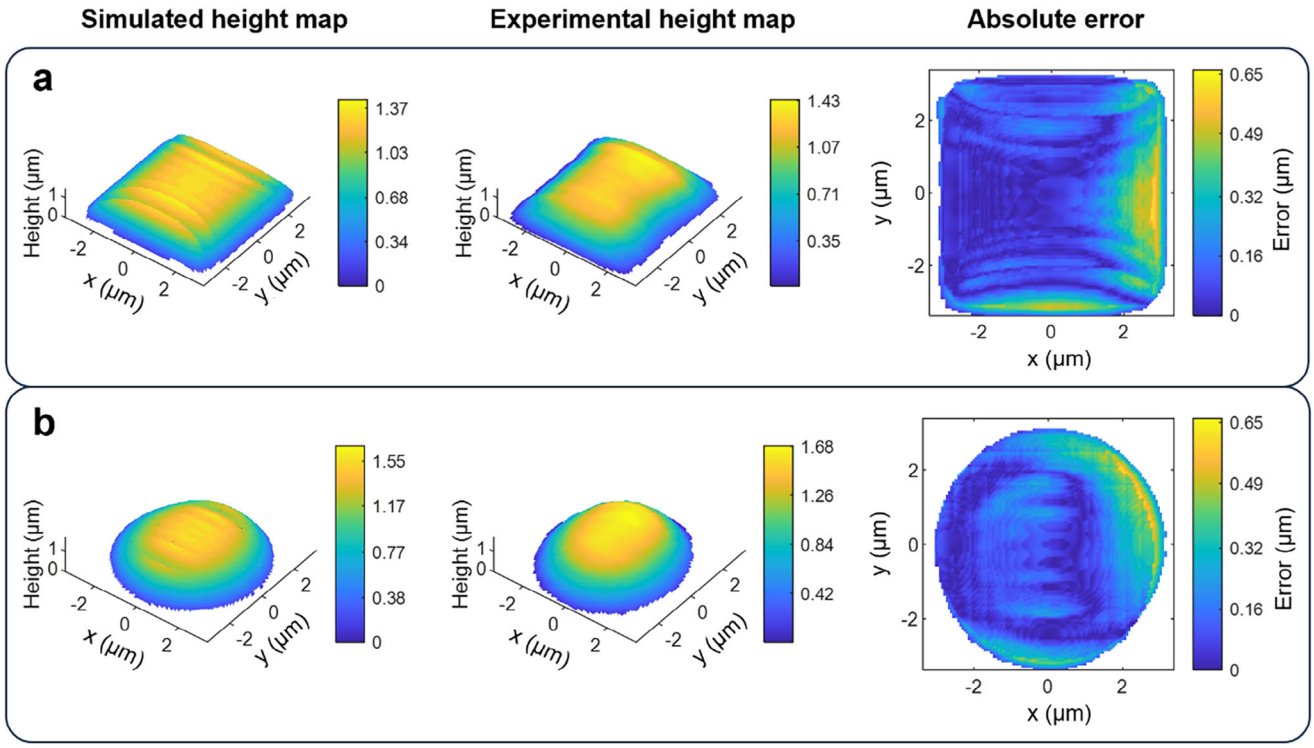

Figure 3. Comparison of experimental and simulated height maps for a) a 6.75 × 6.75 μm rectangle and b) a 6.75 μm diameter circle. Simulated maps are obtained from the highest *z*-coordinate where monomer conversion exceeds the threshold, while experimental maps are measured using quantitative phase imaging (QPI). Absolute error maps show differences between simulation and experiment, with mean errors of 136 nm for the rectangle printed at 140.4 W cm^{-2} with 1500 μs exposure, and 134 nm for the circle printed at 130.3 W cm^{-2} with 2100 μs exposure.

processed QPI images. The smallest size of the printed material that can be observed at threshold differs for different projected circle diameters. The threshold intensity, therefore, simply indicates the intensity below which no printed material is observed in the QPI image. In the model, the degree of monomer conversion was quantified as the ratio of converted monomer *C* in Equation (13) to the initial monomer concentration. A spatial point was considered printed if monomer conversion at that point exceeded 20%.[27,43,56] Below the simulated threshold intensity, there is no location within the simulated volume where the monomer conversion exceeds this conversion threshold.

Figure 2b shows the threshold intensity vs circle diameter relationship obtained experimentally and through simulations. The experimental average intensity values were measured with a step size of ≈10 W cm^{-2}. The error bars in experimental data represent the associated uncertainty (± step size/2). At small diameters, radicals generated during the fixed 1100 μs exposure are rapidly quenched by oxygen, requiring high laser intensity for successful printing. As the diameter increases, more radicals are available from larger areas to sustain polymerization despite oxygen inhibition, thereby lowering the intensity requirement. This trend eventually plateaus, as insufficient radical generation at low intensity cannot overcome oxygen inhibition regardless of circle size or exposure. Both experimental and simulation results follow this characteristic behavior. The deviations observed in the experimental data may be attributed to the pulse-to-pulse intensity fluctuations (±7%) in the laser output, which become non-negligible given the limited number of pulses used in this experiment (1100 μs, corresponding to ≈6 pulses). The overall intensity resulting from such fluctuations alters the number of radicals available to counter oxygen inhibition and sustain monomer conversion, thereby increasing or decreasing the area where sufficient monomer conversion is achieved.

For a uniformly bright pattern projected onto the DMD, the printed layer would ideally exhibit a flat and uniform profile. In practice, however, the layers show corner rounding, feature under-polymerization, and asymmetric distortions, producing dome-like structures, as shown in Figure 3.

The first column of Figure 3 shows simulated height maps, obtained by tracking the *z*-position at each (*x*, *y*) coordinate where monomer conversion reaches the 20% threshold. The middle column presents experimental height maps, measured immediately after printing using the in situ QPI method and processed with an edge detection algorithm. The right column compares experimental and simulated height maps, displaying the mean absolute error at each spatial location. Figure 3a corresponds to a 6.75 μm × 6.75 μm rectangle printed at 140.4 W cm^{-2} average intensity and 1500 μs exposure, and Figure 3b corresponds to a circle of 6.75 μm diameter printed at 130.3 W cm^{-2} average intensity and 2100 μs exposure. In both cases, the mean absolute error between experiment and simulation is ≈140 nm, demonstrating that the model reliably captures experimental trends. It is also noticed that although the projected patterns are symmetric, both experimental and simulated results reveal asymmetric structures with larger dimensions along the *y*-axis. This asymmetry arises from DMD diffraction, which produces higher peak intensities

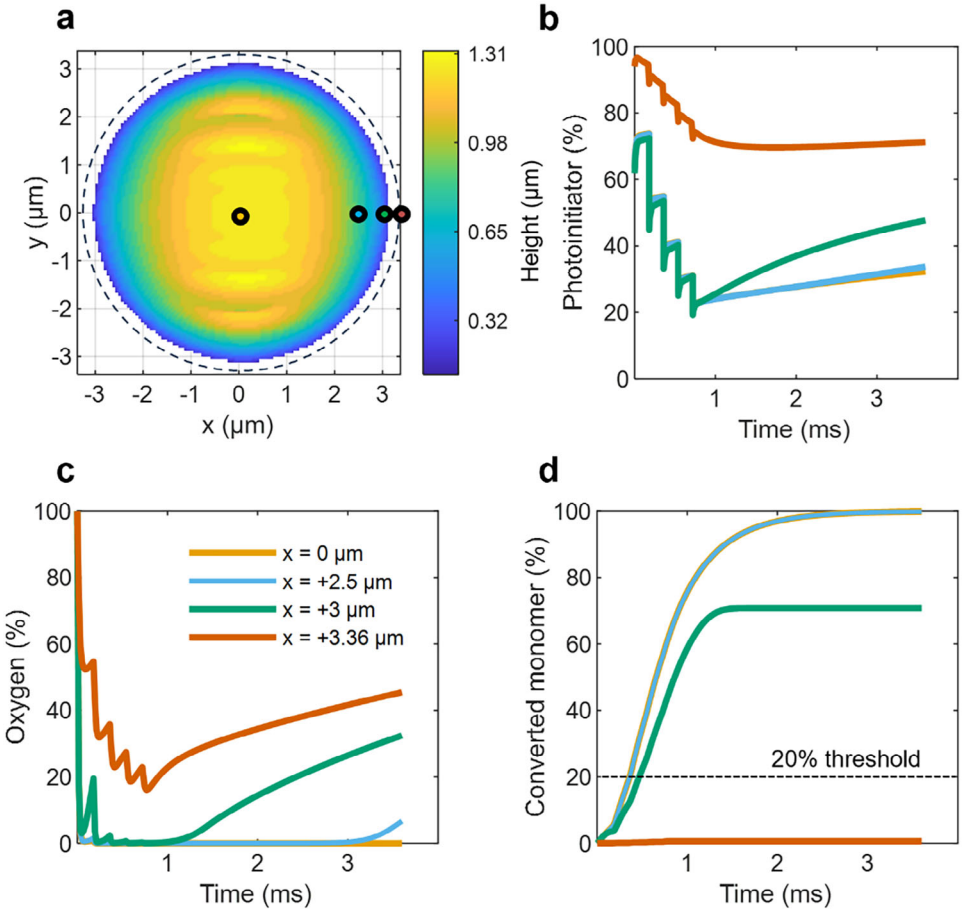

Figure 4. Temporal evolution of the reaction species during printing of a 6.75 μm diameter circle at 160.4 W cm^{-2} average intensity and 900 μs exposure. a) Simulated height map showing radial variation in structure height and reduced final shape. b) Temporal evolution of photoinitiator concentration at different radial positions. c) Temporal evolution of oxygen concentration at the same positions. d) Corresponding monomer conversion profiles. Subfigures (b)–(d) share a common legend.

along the top and bottom horizontal edges, as can be seen in Figure 1d,e. The increased intensity supplies more radicals to overcome oxygen inhibition in this direction, thereby enhancing polymerization and leading to asymmetric growth. Additionally, a continuous reduction in feature size along the *z*-axis, from center to edge, produces a dome-shaped structure due to oxygen inhibition, consistently observed both in experiment and simulation. For all plots, the *x*-axis and *y*-axis limits are set to match the projected pattern dimensions (6.75 μm in each direction), highlighting the reduction in feature size along the boundary. Similar results were observed across nine different intensity and exposure conditions for both circular and rectangular patterns, with the model reliably reproducing the results with a mean absolute error of ≈150 nm.

3.2. Dynamics of Oxygen Diffusion and Inhibition

To investigate the role of oxygen in feature size reduction and polymerization inhibition at the perimeter, we analyzed the temporal evolutions of reaction species under different intensity and exposure conditions for both circular and rectangular patterns. As a representative case, we examined the time-dependent concentration changes during the fabrication of a 6.75 μm diameter circle printed at 160.4 W cm^{-2} average intensity with a 900 μs exposure. The relatively low number of pulses (5 pulses) in this condition facilitates the study of pulse-to-pulse variations, while the circular geometry provides a clear basis for identifying feature size reduction. The simulated height map in Figure 4a reveals a reduction in structure height along the radial direction and a loss of feature size beyond a ≈3 μm radius, resulting in a final printed feature of only ≈6 μm instead of the projected 6.75 μm diameter indicated by the dotted circle. The underlying mechanism is elucidated by examining variations in photoinitiator, oxygen, and converted monomer concentrations as functions of time and radial location, as shown in Figure 4b–d. In Figure 4b, photoinitiator molecules are periodically consumed by pulsed excitation every 200 μs, followed by replenishment through diffusion from the surrounding region. However, even at the center location ($x = 0$ μm), the concentration never approaches zero. Thus, the reduction in photoinitiator concentration cannot solely explain the geometric deviations observed in this work. In contrast, oxygen plays a critical role in limiting the spatial extent of polymerization, as illustrated in Figure 4c,d. At the circle center ($x = 0$ μm),

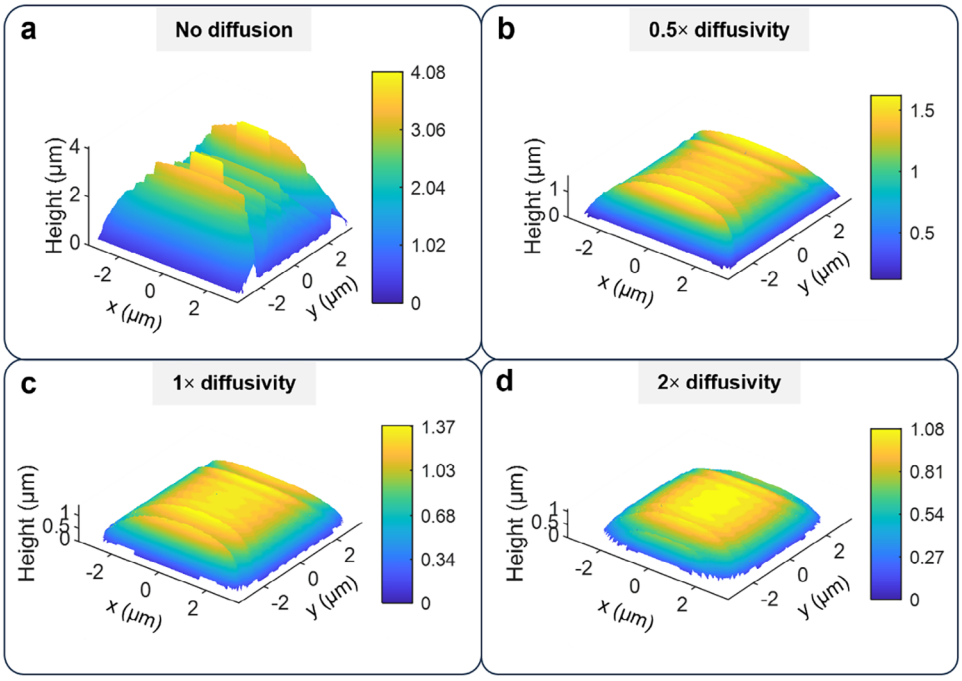

Figure 5. Effects of oxygen diffusion on a 6.75 × 6.75 μm rectangle printed at 140.4 W cm^{-2} average intensity and 1500 μs exposure. The baseline oxygen diffusivity value of 7.48 × 10^{-10} m^2 s^{-1} is taken from Table 1. a) Without oxygen diffusion, polymerization is less confined in height, and diffraction-induced deviations are amplified. b,c) Increasing oxygen diffusion (0.5× diffusivity and 1× diffusivity) confines the structure in the *z*-direction but causes loss of sharp features at the corners and asymmetric polymerization. d) Excessive diffusion (2× diffusivity) results in substantial feature loss in both height and lateral dimensions.

oxygen is depleted to near zero within two pulses (≈400 μs), enabling monomer conversion above the threshold. This timescale is consistent with the intrinsic polymerization time of ≈300 μs reported for MPP.[27] At intermediate positions ($x = +2.5$ μm to $x = +3$ μm), oxygen is also sufficiently consumed to permit polymerization, though continuous diffusion from the surroundings reduces the achievable structure height. At the outer boundary ($x = 3.36$ μm), however, oxygen is never fully depleted, preventing the monomer conversion from exceeding the threshold. Consequently, no stable polymerization occurs at this location, leading to the observed under-sizing of the printed feature relative to the projected DMD pattern.

Although oxygen inhibition contributes to geometric deviations in PMPL, it also plays a beneficial role by confining polymerization axially and smoothing artifacts of diffraction in the intensity profile. To investigate the coupled effects of oxygen inhibition and diffraction, **Figure 5** illustrates the influence of oxygen diffusivity ($d_z = 7.48 \times 10^{-10}$ m^2 s^{-1}), taken from model parameters listed in Table 1, on a rectangular structure printed at 140.4 W cm^{-2} with a 1500 μs exposure time. In the absence of oxygen diffusion, polymerization begins immediately after local oxygen depletion and proceeds uncontrollably until all generated radicals are consumed, thereby exacerbating the diffraction effects, as shown in Figure 5a. As oxygen diffusivity increases, polymerization becomes increasingly confined, with inhibition suppressing reactions in regions of lower intensity where fewer radicals are generated. This confinement reduces uneven surfaces caused by diffraction but also results in a gradual loss of sharp features, particularly at the corners, as evident in Figure 5b,c. Furthermore, diffraction introduces intensity variations in the projected pattern, with the highest intensity occurring at the top and bottom horizontal edges as seen in Figure 1d,e. The increased radical generation at these edges reduces the effectiveness of oxygen inhibition along the *y*-axis relative to the *x*-axis, producing asymmetric structures consistent with the distortions observed experimentally in Figure 3. At very high oxygen diffusivity, polymerization is excessively suppressed, leading to substantial feature size reduction along both axes, as shown in Figure 5d. These results highlight the dual role of oxygen diffusion. While it suppresses uncontrolled polymerization and partially compensates for diffraction artifacts, excessive diffusion compromises feature fidelity. Counter-strategies are therefore needed to balance and mitigate the coupled effects of oxygen inhibition and diffraction in PMPL.

3.3. Proposed Strategy for Printing a Uniform and Symmetric Structure

To achieve a printed layer that better matches the projected pattern, we propose two key strategies. First, oxygen must be depleted from the exposed area during projection to prevent under-polymerization and corner rounding. Second, asymmetric distortions arising from DMD diffraction and oxygen inhibition must be corrected by projecting modified patterns with inherent asymmetry. These strategies are illustrated in **Figure 6** for both rectangular and circular features. Figure 6a,b shows the compensation approach for a 6.75 × 6.75 μm rectangle, while Figure 6c,d shows

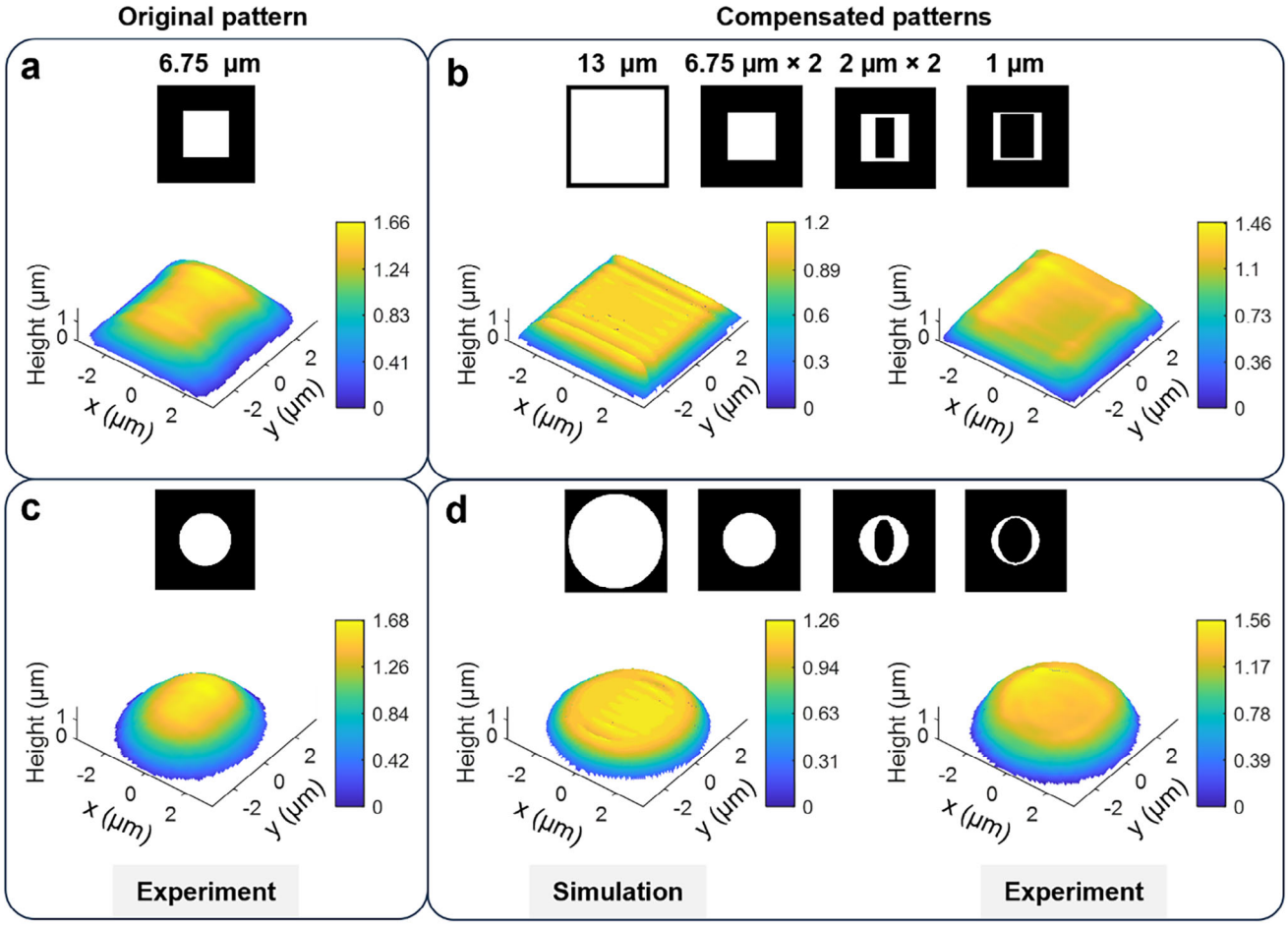

Figure 6. Compensation strategies for rectangular and circular features in PMPL. a) Uncompensated and b) compensated 6.75 × 6.75 μm rectangle results, and c) uncompensated and d) compensated 6.75 μm diameter circle results. In (b) and (d), model predictions using the modified patterns are shown on the left, and the experimental results for the same modified patterns are shown on the right. The compensation strategy employs six sequentially projected patterns with varying exposure times, shown at the top of (b) and (d). A 13 μm pre-exposure pattern to deplete oxygen, projected for 398 μs, two 6.75 μm patterns to print the target geometry, and three asymmetric ring-shaped patterns, all projected at 798 μs each. For the asymmetric rings, the outer dimensions match the intended feature, while inner borders are adjusted along x and y to introduce asymmetry (2 μm rings: 2 μm × 1 μm; 1 μm ring: 1 μm × 0.5 μm). The unmodified structures in (a) and (c) are printed at 130.3 W cm^{-2} average intensity for 2100 μs, while the compensated patterns in (b) and (d) are printed at 120.3 W cm^{-2}.

the results for a 6.75 μm diameter circle. In each case, the left column shows experimental prints from unmodified patterns projected with 130.3 W cm^{-2} average intensity for 2100 μs. The right column shows results using compensated patterns designed to correct for oxygen inhibition and diffraction. The left image in the right column presents model predictions using the modified patterns, while the right image shows experimentally improved results achieved with these modifications. The projected patterns used in each case are also displayed, with white and black regions representing on/off pixels in the DMD, respectively.

The compensation strategy employs six sequentially projected patterns at 120.3 W cm^{-2} with varying exposure times. Since the DMD operates at 4 kHz (≈250 μs per pattern), per-pattern exposure times of 398 μs (2 pulses) and 798 μs (4 pulses) were selected to ensure consistent pulse counts with the 5 kHz printing laser. From Figure 4, two pulses at 160.4 W cm^{-2} are sufficient to deplete oxygen from a region and achieve monomer conversion above the 20% threshold. Thus, using a lower intensity, two pulses can sufficiently remove oxygen without inducing polymerization above the threshold. Based on this principle, the first 13 μm pattern acts as a pre-exposure, depleting oxygen over a larger region without polymerizing with two pulses (398 μs), ensuring that oxygen does not diffuse back before the subsequent intended patterns are projected. The 13 μm size is chosen to fit within the simulated volume, but any sufficiently large pre-exposure pattern could serve the same purpose. In the absence of in-situ power control, the same intensity is used for each laser pulse, and the total dose per pattern is adjusted by changing the exposure time per pattern. The remaining compensated patterns are each projected for 798 μs (4 pulses). The second and third 6.75 μm target patterns polymerize the intended rectangular or circular feature. The fourth, fifth, and sixth patterns are asymmetric ring-shaped modifications introduced to correct both diffraction and oxygen inhibition. Each ring-shaped pattern has outer

dimensions matching the intended feature size, while the inner dimensions are adjusted differently along x and y to correct asymmetry. The fourth and fifth rings have a 2 μm border along x and 1 μm along y, while the sixth pattern has a 1 μm border along x and 0.5 μm along y. Since the total exposure of the compensated patterns is higher than that of the original patterns, which are projected for 2100 μs at an average intensity of 130.3 W cm^{-2}, the compensated patterns are projected at a lower average intensity of 120.3 W cm^{-2} to maintain a comparable total dose and avoid over-polymerization. In all plots, the x-y axes correspond to the dimensions of the original pattern projected onto the DMD. The results show that compensated patterns, particularly the pre-exposure step, effectively mitigate under-polymerization and corner rounding caused by oxygen inhibition. The asymmetric rings produce more symmetric structures, countering the distortions arising from oxygen inhibition and diffraction. They also reduce the gradual decrease in feature height along the z-axis, which otherwise produces dome-shaped profiles. Compared to prints from unmodified patterns, the compensated approach yields a flatter structure with improved fidelity. Some residual curvature remains at the edges, indicating that further optimization is needed to achieve sharper boundaries. Nonetheless, the enhanced experimental results in Figure 6 highlight the effectiveness of sequential compensation in controlling feature geometry in PMPL. This work provides a general framework for physics-guided optimization. Future development can include machine learning and other advanced tools to further optimize the compensation process in PMPL.

4. Conclusion

In this work, we investigated the fundamental origins of geometric deviations in PMPL. By integrating a numerical framework that combines optical modeling with reaction–diffusion simulations of photopolymerization kinetics, we identified oxygen inhibition and diffusion and DMD diffraction as the primary factors driving printed feature size inaccuracies, sharp feature loss, and asymmetries. Comparison between simulations and experimental height maps confirmed the predictive capability of the model, with mean absolute errors between simulated and experimental height maps on the order of ≈150 nm. Systematic analysis of threshold intensity vs circle diameter and time-dependent concentrations of reaction species confirmed the role of oxygen in controlling printability in PMPL, similar to conventional MPP across different intensity and exposure doses. Studies of oxygen diffusivity highlighted its dual role. While oxygen confines polymerization and suppresses uncontrolled growth, it also contributes to the loss of sharp features and reduction in feature size. The coupled effects of oxygen diffusion and DMD diffraction in producing asymmetric distortions were also demonstrated. Building on these insights, we proposed compensation strategies that combine a pre-exposure step to locally deplete oxygen with subsequent asymmetric pattern modifications to correct diffraction-induced distortions. Both simulations and experimental results show the promise of these approaches in improving the geometric accuracy of printed microstructures. Overall, this study establishes a physics-based foundation for understanding and compensating distortions in PMPL. By bridging mechanistic modeling with experimental validation, the framework presented here provides a pathway toward more accurate 3D printing at high speed. Future work can extend this approach to more complex geometries and adaptive, data-driven compensation schemes for scalable nanofabrication.

5. Experimental Section

Experimental Setup: A 5 kHz Ti-sapphire regenerative amplifier (Coherent Legend Elite Duo USX) with ≈40 fs pulse duration, 30 nm bandwidth, and 800 nm center wavelength served as the excitation source. Laser power was controlled using a half-wave plate (Thorlabs AHWP10M-580) and a polarizing beam splitter cube (Thorlabs PBS25-780). The beam was collimated and expanded to ≈12 mm diameter using a lens pair consisting of a concave lens (f = −125 mm, Edmund Optics #49-539) and a convex lens (f = 150 mm, Thorlabs LA1417-B). After passing through a πShaper (AdlOptica πShaper 12_12_TiS_HP), the beam was incident on a DMD (DLP4500NIR) at an angle of ≈24° relative to the surface normal. Diffracted light from the DMD was collected with an achromatic doublet (f = 180 mm, Thorlabs AC508-180-AB) and focused at the back focal plane of a 100× oil immersion objective lens (Nikon, 1.49 NA). Structures were printed in a dip-in configuration and positioned using a 3-axis air bearing stage (Aerotech ABL1000 series). All laser powers were measured after the polarizing beam splitter, with ≈7% of the measured power transmitted to the print plane. Average intensity values were calculated based on this transmitted power, the 12 mm beam diameter incident on the DMD, and the system (de)magnification of 90. The printed structures were imaged through a CMOS camera (FLIR GS3-U3-32S4M) and analyzed with the in situ quantitative phase imaging (QPI) method.[55]

Photoresists: The photoresist was prepared by adding the photoinitiator (2E,6E)-2,6-Bis (4-(dibutylamino) benzylidene)-4-methylcyclohexanone (BBK) to the monomer, pentaerythritol triacrylate (PETA, Sigma-Aldrich), at a concentration of 0.38 mol%, which is the highest concentration that can be homogeneously dissolved, followed by sonication for 4 h. BBK was synthesized via an aldol condensation reaction.[18,57]

Acknowledgements

The authors gratefully acknowledge support from the U.S. National Science Foundation under grant CMMI-2135585. Jason Johnson acknowledges support from the U.S. National Science Foundation Graduate Research Fellowship Program (GRFP) under grant DGE-1842166. The authors also thank Prof. Bryan Boudouris and Kaushik Baruah for the synthesis of the BBK photoinitiator.

Conflict of Interest

The authors declare no conflict of interest.

Data Availability Statement

The data that support the findings of this study are available from the corresponding author upon reasonable request.

Keywords

3D printing, additive manufacturing, modeling and simulation, multiphoton polymerization, projection multiphoton lithography

Received: September 29, 2025
Revised: December 20, 2025
Published online:

[1] S. O'Halloran, A. Pandit, A. Heise, A. Kellett, *Adv. Sci.* **2023**, *10*, 2204072.
[2] S. Kawata, H.-B. Sun, T. Tanaka, K. Takada, *Nature* **2001**, *412*, 697.
[3] P. Somers, A. Münchinger, S. Maruo, C. Moser, X. Xu, M. Wegener, *Nat. Rev. Phys.* **2024**, *6*, 99.
[4] E. Skliutas, G. Merkininkaitė, S. Maruo, W. Zhang, W. Chen, W. Deng, J. Greer, G. von Freymann, M. Malinauskas, *Nat. Rev. Methods Prim.* **2025**, *5*, 15.
[5] H. Wang, W. Zhang, D. Ladika, H. Yu, D. Gailevičius, H. Wang, C.-F. Pan, P. N. S. Nair, Y. Ke, T. Mori, J. Y. E. Chan, Q. Ruan, M. Farsari, M. Malinauskas, S. Juodkazis, M. Gu, J. K. W. Yang, *Adv. Funct. Mater.* **2023**, *33*, 2214211.
[6] M. Marini, A. Nardini, R. Martínez Vázquez, C. Conci, M. Bouzin, M. Collini, R. Osellame, G. Cerullo, B. S. Kariman, M. Farsari, E. Kabouraki, M. T. Raimondi, G. Chirico, *Adv. Funct. Mater.* **2023**, *33*, 2213926.
[7] D. Gonzalez-Hernandez, S. Varapnickas, A. Bertoncini, C. Liberale, M. Malinauskas, *Adv. Opt. Mater.* **2023**, *11*, 2201701.
[8] G. T. Iványi, B. Nemes, I. Gróf, T. Fekete, J. Kubacková, Z. Tomori, G. Bánó, G. Vizsnyiczai, L. Kelemen, *Adv. Mater.* **2024**, *36*, 2401115.
[9] C. A. Spiegel, M. Hippler, A. Münchinger, M. Bastmeyer, C. Barner-Kowollik, M. Wegener, E. Blasco, *Adv. Funct. Mater.* **2020**, *30*, 1907615.
[10] J. Song, C. Michas, C. S. Chen, A. E. White, M. W. Grinstaff, *Adv. Healthcare Mater.* **2020**, *9*, 1901217.
[11] A. Selimis, V. Mironov, M. Farsari, *Microelectron. Eng.* **2015**, *132*, 83.
[12] T. Frenzel, M. Kadic, M. Wegener, *Science* **2017**, *358*, 1072.
[13] M. P. Jeske, W. Zhang, M. Anthamatten, *Adv. Mater. Technol.* **2022**, *7*, 2101725.
[14] P. Kiefer, V. Hahn, S. Kalt, Q. Sun, Y. M. Eggeler, M. Wegener, *Light: Adv. Manufact.* **2024**, *4*, 28.
[15] A. Balena, M. Bianco, F. Pisanello, M. De Vittorio, *Adv. Funct. Mater.* **2023**, *33*, 2211773.
[16] L. Zhang, C. Wang, C. Zhang, Y. Xue, Z. Ye, L. Xu, Y. Hu, J. Li, J. Chu, D. Wu, *Nano Lett.* **2024**, *24*, 2671.
[17] S. K. Saha, D. Wang, V. H. Nguyen, Y. Chang, J. S. Oakdale, S.-C. Chen, *Science* **2019**, *366*, 105.
[18] P. Somers, Z. Liang, J. E. Johnson, B. W. Boudouris, L. Pan, X. Xu, *Light Sci. Appl.* **2021**, *10*, 199.
[19] J. R. Tumbleston, D. Shirvanyants, N. Ermoshkin, R. Janusziewicz, A. R. Johnson, D. Kelly, K. Chen, R. Pinschmidt, J. P. Rolland, A. Ermoshkin, E. T. Samulski, J. M. DeSimone, *Science* **2015**, *347*, 1349.
[20] D. A. Walker, J. L. Hedrick, C. A. Mirkin, *Science* **2019**, *366*, 360.
[21] Q. Ge, Z. Li, Z. Wang, K. Kowsari, W. Zhang, X. He, J. Zhou, N. X. Fang, *Int. J. Extreme Manufact.* **2020**, *2*, 022004.
[22] D. Kim, P. T. C. So, *Opt. Lett.* **2010**, *35*, 1602.
[23] Y.-C. Li, L.-C. Cheng, C.-Y. Chang, C.-H. Lien, P. J. Campagnola, S.-J. Chen, *Opt. Express* **2012**, *20*, 19030.
[24] A. Ovsianikov, X. Shizhou, M. Farsari, M. Vamvakaki, C. Fotakis, B. N. Chichkov, *Opt. Express* **2009**, *17*, 2143.
[25] A. S. Jariwala, F. Ding, A. Boddapati, V. Breedveld, M. A. Grover, C. L. Henderson, D. W. Rosen, *Rapid Prototyp J.* **2011**, *17*, 168.
[26] J. E. Johnson, I. R. Jamil, L. Pan, G. Lin, X. Xu, *Light Sci. Appl.* **2025**, *14*, 56.
[27] J. B. Mueller, J. Fischer, F. Mayer, M. Kadic, M. Wegener, *Adv. Mater.* **2014**, *26*, 6566.
[28] A. K. O'Brien, C. N. Bowman, *Macromol. Theory Simul.* **2006**, *15*, 176.
[29] S. C. Ligon, B. Husár, H. Wutzel, R. Holman, R. Liska, *Chem. Rev.* **2014**, *114*, 557.
[30] J. E. Johnson, Y. Chen, X. Xu, *Opt. Express* **2022**, *30*, 26824.
[31] A. I. Akash, J. E. Johnson, F. C. Arentz, X. Xu, *Opt. Express* **2024**, *32*, 25892.
[32] M. Sun, H. Cheng, P. Golvari, S. M. Kuebler, X. Yu, M. Zhang, *Addit. Manuf.* **2022**, *60*, 103241 .
[33] V. Sedova, F. Ogor, J. Rovera, O. Tsilipakos, L. Lemberg, K. Heggarty, A. Erdmann, *SPIE* **2024**, *13023*, 1302309.
[34] H. Wang, H. Wang, W. Zhang, J. K. W. Yang, *ACS Nano* **2020**, *14*, 10452.
[35] T. Aderneuer, O. Fernández, R. Ferrini, *Opt. Express* **2021**, *29*, 39511.
[36] R. Pingali, S. K. Saha, *J. Micro Nano Sci. Eng.* **2024**, *12*, 011001.
[37] R. Pingali, S. K. Saha, *J. Manuf. Sci. Eng.* **2021**, *144*, 021011.
[38] I. R. Jamil, J. E. Johnson, X. Xu, *Addit. Manuf.* **2025**, *110*, 104929.
[39] J. Johnson, *Active Machine Learning for Projection Multi-Photon Lithography*, Purdue University Graduate School, West Lafayette, IN **2025**.
[40] J. W. Goodman, *Introduction to Fourier Optics*, Roberts and Company Publishers, Greenwood Village, CO **2005**.
[41] A. Mauri, P. Kiefer, W. Wenzel, M. Kozlowska, *Macromol. Rapid Commun.* **2025**, *46*, 2500231.
[42] P. Somers, Z. Liang, T. Chi, J. E. Johnson, L. Pan, B. W. Boudouris, X. Xu, *Nanophotonics* **2023**, *12*, 1571.
[43] L. Yang, A. Münchinger, M. Kadic, V. Hahn, F. Mayer, E. Blasco, C. Barner-Kowollik, M. Wegener, *Adv. Opt. Mater.* **2019**, *7*, 1901040.
[44] N. Liaros, S. A. Gutierrez Razo, M. D. Thum, H. M. Ogden, A. N. Zeppuhar, S. Wolf, T. Baldacchini, M. J. Kelley, J. S. Petersen, D. E. Falvey, A. S. Mullin, J. T. Fourkas, *iScience* **2022**, *25*, 103600.
[45] J. Z. Bloh, *Front. Chem.* **2019**, *7*, 128.
[46] J.-T. Lin, H.-W. Liu, K.-T. Chen, D.-C. Cheng, *Front. Chem.* **2019**, *7*, 760.
[47] M. Stavrou, D. Ladika, E. Skliutas, V. Jukna, D. Gray, M. Farsari, S. Juodkazis, M. Malinauskas, *Nanophotonics* **2025**, *14*, 2981.
[48] J. Fischer, J. B. Mueller, J. Kaschke, T. J. A. Wolf, A.-N. Unterreiner, M. Wegener, *Opt. Express* **2013**, *21*, 26244.
[49] M. R. Gleeson, S. Liu, J. Guo, J. T. Sheridan, *J. Opt. Soc. Am. B* **2010**, *27*, 1804.
[50] H. Duran, S. Meng, N. Kim, J. Hu, T. Kyu, L. V. Natarajan, V. P. Tondiglia, T. J. Bunning, *Polymer (Guildf)* **2008**, *49*, 534.
[51] J. Christmann, X. Allonas, C. Ley, A. Ibrahim, C. Croutxé-Barghorn, *Macromol. Chem. Phys.* **2017**, *218*, 1600597.
[52] K. Taki, *Polymers (Basel)* **2020**, *12*, 875.
[53] Z. Li, N. Pucher, K. Cicha, J. Torgersen, S. C. Ligon, A. Ajami, W. Husinsky, A. Rosspeintner, E. Vauthey, S. Naumov, T. Scherzer, J. Stampfl, R. Liska, *Macromolecules* **2013**, *46*, 352.
[54] R. Mundt, T. Villnow, C. T. Ziegenbein, P. Gilch, C. Marian, V. Rai-Constapel, *Phys. Chem. Chem. Phys.* **2016**, *18*, 6637.
[55] R. Zvagelsky, P. Kiefer, J. Weinacker, M. Wegener, *ACS Photonics* **2023**, *10*, 2901.
[56] F. Burmeister, S. Steenhusen, R. Houbertz, U. D. Zeitner, S. Nolte, A. Tünnermann, *J. Laser Appl.* **2012**, *24*, 042014.
[57] P. Kiefer, V. Hahn, M. Nardi, L. Yang, E. Blasco, C. Barner-Kowollik, M. Wegener, *Adv. Opt. Mater.* **2020**, *8*, 2000895.